



**HAL**  
open science

# Explicit and viscosity-independent immersed-boundary scheme for the lattice Boltzmann method

Simon Gsell, Umberto d'Ortona, Julien Favier

► **To cite this version:**

Simon Gsell, Umberto d'Ortona, Julien Favier. Explicit and viscosity-independent immersed-boundary scheme for the lattice Boltzmann method. *Physical Review E*, 2019, 100 (3), 10.1103/PhysRevE.100.033306 . hal-02339475


**HAL Id: hal-02339475**

**<https://hal.science/hal-02339475>**

Submitted on 4 Nov 2019

**HAL** is a multi-disciplinary open access archive for the deposit and dissemination of scientific research documents, whether they are published or not. The documents may come from teaching and research institutions in France or abroad, or from public or private research centers.

L'archive ouverte pluridisciplinaire **HAL**, est destinée au dépôt et à la diffusion de documents scientifiques de niveau recherche, publiés ou non, émanant des établissements d'enseignement et de recherche français ou étrangers, des laboratoires publics ou privés.

**Explicit and viscosity-independent immersed-boundary scheme for the lattice Boltzmann method**Simon Gsell <sup>\*</sup>, Umberto D'Ortona , and Julien Favier  
*Aix Marseille Univ, CNRS, Centrale Marseille, M2P2, Marseille, France* (Received 21 June 2019; published 11 September 2019)

Viscosity independence of lattice-Boltzmann methods is a crucial issue to ensure the physical relevancy of the predicted macroscopic flows over large ranges of physical parameters. The immersed-boundary (IB) method, a powerful tool that allows one to immerse arbitrary-shaped, moving, and deformable bodies in the flow, suffers from a boundary-slip error that increases as a function of the fluid viscosity, substantially limiting its range of application. In addition, low fluid viscosities may result in spurious oscillations of the macroscopic quantities in the vicinity of the immersed boundary. In this work, it is shown mathematically that the standard IB method is indeed not able to reproduce the scaling properties of the macroscopic solution, leading to a viscosity-related error on the computed IB force. The analysis allows us to propose a simple correction of the IB scheme that is local, straightforward and does not involve additional computational time. The derived method is implemented in a two-relaxation-time D2Q9 lattice-Boltzmann solver, applied to several physical configurations, namely, the Poiseuille flow, the flow around a cylinder towed in still fluid, and the flow around a cylinder oscillating in still fluid, and compared to a noncorrected immersed-boundary method. The proposed correction leads to a major improvement of the viscosity independence of the solver over a wide range of relaxation times (from 0.5001 to 50), including the correction of the boundary-slip error and the suppression of the spurious oscillations. This improvement may considerably extend the range of application of the IB lattice-Boltzmann method, in particular providing a robust tool for the numerical analysis of physical problems involving fluids of varying viscosity interacting with solid geometries.

DOI: [10.1103/PhysRevE.100.033306](https://doi.org/10.1103/PhysRevE.100.033306)**I. INTRODUCTION**

The lattice-Boltzmann method, issued from the discretization of the Boltzmann equation, has become a popular numerical method to simulate fluid flows [1,2]. Even though it statistically describes the dynamics of the microscopic fluid particles—it is said that the flow is described at the mesoscopic scale—the lattice-Boltzmann method can accurately predict the flow behavior at the macroscopic scale [3–5]. This is supported by the Chapman-Enskog analysis [6], which formally derives the Navier-Stokes equations from the Boltzmann equation.

However, the physical relevancy of the predicted macroscopic flow may be dependent on a number of conditions regarding the numerical parameters. Especially, the relaxation time, involved in the collision operator of the Boltzmann equation and directly related to the fluid viscosity, should be varied with caution as it often impacts the macroscopic solution [7]. This may lead to unphysical behaviors, since the dynamics of the macroscopic flow should remain independent of the viscosity as long as the governing nondimensional physical parameters are kept constant. The Bhatnagar-Gross-Krook (BGK) collision operator [8], often considered as the simplest and most convenient model, has proved to violate this viscosity-independence principle [9]. This considerably limits the range of relaxation times that can be used in computations, eventually limiting the range of appli-

cations of the lattice-Boltzmann method. More sophisticated collision models, involving multiple relaxation times [10], should thus be considered; in particular, a two-relaxation-time model is employed in this work [11,12]. However, viscosity-dependent errors may still arise from boundary conditions.

While the implementation of no-slip conditions on lattice-fitted boundaries may be straightforward using bounce-back [7,13–15] or wet-node [16] approaches, the inclusion of curved walls in the flow may remain challenging, especially in the case of moving and/or deformable geometries. The immersed-boundary (IB) method is a promising tool for the simulation of such configurations. This method, first developed for Navier-Stokes fluid solvers [17,18], allows one to model the body-flow interactions through the addition of a source term in the flow-momentum equation, enforcing the no-slip condition in the vicinity of the body. Even though the IB method has been successfully implemented in several lattice-Boltzmann solvers [19–23], it still presents some limitations. In particular, Le and Zhang [24] have pointed out the undesired effect of the fluid viscosity on the flow solution: the velocity error close to the solid boundary, called boundary slip, increases as a function of the relaxation time. As a result, the standard IB method can hardly be used for the simulation of low-Reynolds-number problems, as encountered in many biological systems. Indeed, if the fluid viscosity cannot be increased, the Reynolds number is generally decreased by decreasing the flow velocity, thus increasing the cost of the computations. In addition, these systems often involve non-Newtonian fluids, i.e., fluids of varying viscosity. In

<sup>\*</sup>simon.gsell@univ-amu.fr

lattice-Boltzmann solvers, these fluids are usually modeled by varying the relaxation time according to the local fluid viscosity [25]. Local variations of the viscosity may thus impact the local accuracy of the IB method. The simulation of yield-stress fluids, for instance, may involve very large relaxation times to model the behavior of solid-like phases. The viscosity dependence of lattice-Boltzmann methods may also be critical for the simulation of high Reynolds number flows, since the decrease of the relaxation time often leads to stability issues [26]. In these contexts, the development of IB methods ensuring numerical reliability for any fluid viscosity is crucial. Seta *et al.* [22] have shown that the boundary-slip error can be corrected using an implicit IB method. However, this approach substantially increases the complexity of the implementation and the cost of the computations, since it involves the solving of linear systems at each time step. As this additional cost drastically increases as a function of the number of IB markers, this method may be barely suitable for systems involving a large number of immersed bodies. Moreover, the high nonlocality of implicit methods is expected to alter the potential scalability of a parallelized lattice-Boltzmann IB solver. In the following, an alternative explicit correction of the IB method is proposed.

This work is based on a two-relaxation-time IB lattice-Boltzmann method, described in Sec. II. In Sec. III a general mathematical formalism is proposed to describe the influence of the relaxation time on the boundary slip. An explicit correction of the IB forcing is then derived in order to achieve the viscosity independence of the solution. The effective influence of the relaxation time is analyzed numerically, in Sec. IV, using the standard and corrected IB methods, for several two-dimensional physical configurations: the Poiseuille flow, the flow around a cylinder towed in a periodic channel, and the flow around an oscillating cylinder. Finally, the principal conclusions of this work are summarized in Sec. V.

## II. NUMERICAL METHOD

The general numerical approach is presented in the following. The two-relaxation-time lattice-Boltzmann method is presented in Sec. II A. The IB method is detailed in Sec. II B.

### A. Lattice-Boltzmann method

At the mesoscopic scale, the flow is described by the particle distribution function  $f(\mathbf{x}, \boldsymbol{\xi}, t)$ , which represents the density of fluid particles with velocity  $\boldsymbol{\xi}$  at location  $\mathbf{x}$  and time  $t$ . The dynamics of the distribution function is governed by the Boltzmann equation,

$$\frac{\partial f}{\partial t} + \boldsymbol{\xi} \cdot \nabla f = \Omega(f), \quad (1)$$

where  $\Omega$  is the collision operator. The discretization of (1) in velocity space, physical space, and time leads to the lattice-Boltzmann equation. The velocity space is discretized on a set of velocity vectors  $\{\mathbf{c}_l, l = 0, \dots, Q-1\}$ , where  $Q$  is the number of discrete velocities. In the present work, which focuses only on two-dimensional physical configurations, a  $D2Q9$  velocity set is used, in which the velocity space is

discretized by nine velocities, namely,

$$\mathbf{c}_l = \begin{cases} (0, 0), & l = 0 \\ c \left\{ \cos \left[ \frac{\pi(l-1)}{2} \right], \sin \left[ \frac{\pi(l-1)}{2} \right] \right\}, & l \in [1, 4], \\ \sqrt{2}c \left\{ \cos \left[ \frac{\pi(2l-9)}{4} \right], \sin \left[ \frac{\pi(2l-9)}{4} \right] \right\}, & l \in [5, 8] \end{cases} \quad (2)$$

where  $c$  is the lattice speed, and  $\mathbf{e}_x$  and  $\mathbf{e}_y$  are unit vectors in the  $x$  and  $y$  directions. The particle densities at velocities  $\{\mathbf{c}_l\}$  are represented by the discrete-velocity distribution functions  $\{f_l(\mathbf{x}, t)\}$ , also called particle populations. The macroscopic flow quantities are moments of the particle populations in the velocity space. In particular, the fluid momentum and density write

$$\rho \mathbf{u} = \sum_{l=0}^8 f_l \mathbf{c}_l, \quad \rho = \sum_{l=0}^8 f_l, \quad (3)$$

with  $\rho$  and  $\mathbf{u}$  the fluid density and velocity. Time and space are discretized so that particle populations are transported from one node to a neighboring one during one time step, namely,  $\Delta x/\Delta t = \Delta y/\Delta t = c$ . The associated grid is thus Cartesian and uniform. The grid spacing is denoted by  $\Delta n = \Delta x = \Delta y$ . In the following, all quantities are normalized by  $c$  and  $\Delta t$ , so that  $\Delta n = \Delta t = 1$ . Using this normalization, the lattice-Boltzmann equation writes

$$f_l(\mathbf{x} + \mathbf{c}_l, t + 1) - f_l(\mathbf{x}, t) = \Omega_l(\mathbf{x}, t). \quad (4)$$

The left-hand side of (4) describes the streaming step; the right-hand side is the collision step. Equation (4) is explicit, and the streaming and collision steps can be treated separately, as summarized in Sec. IV A.

A common modeling of the collision term  $\Omega$  is the Bhatnagar-Gross-Krook (BGK) operator [8],

$$\Omega_l^{BGK}(\mathbf{x}, t) = -\frac{1}{\tau} [f_l(\mathbf{x}, t) - f_l^{(eq)}(\mathbf{x}, t)], \quad (5)$$

which relaxes distributions  $\{f_l\}$  towards equilibrium functions  $\{f_l^{(eq)}\}$  at a rate determined by the relaxation time  $\tau$ . The latter relates to the fluid kinematic viscosity,  $\nu = c_s^2(\tau - \frac{1}{2})$ , where  $c_s$  denotes the sound speed, equal to  $1/\sqrt{3}$  using the present normalization. The equilibrium populations are given by

$$f_l^{(eq)} = w_l \rho \left[ 1 + \frac{\mathbf{u} \cdot \mathbf{c}_l}{c_s^2} + \frac{(\mathbf{u} \cdot \mathbf{c}_l)^2}{2c_s^4} - \frac{\mathbf{u} \cdot \mathbf{u}}{2c_s^2} \right]. \quad (6)$$

The weights  $\{w_l\}$  are specific to the velocity set. In the present case ( $D2Q9$  velocity set),  $w_0 = 4/9$ ,  $w_1 = w_2 = w_3 = w_4 = 1/9$ , and  $w_5 = w_6 = w_7 = w_8 = 1/36$ .

The main advantage of the BGK model, its simplicity, is balanced by a critical limitation: while the flow is expected to be accurately simulated for  $\tau \approx 1$ , this accuracy may be significantly altered when the relaxation time departs from unity. The simplest approach to improve the viscosity-independence of the solver is the two-relaxation-time model, employed in this work. This model is based on a decomposition of the populations into symmetric and antisymmetric parts, namely,

$$f_l^+ = \frac{f_l + f_{\bar{l}}}{2}, \quad f_l^- = \frac{f_l - f_{\bar{l}}}{2}, \quad (7a)$$

$$f_l^{(eq)+} = \frac{f_l^{(eq)} + f_{\bar{l}}^{(eq)}}{2}, \quad f_l^{(eq)-} = \frac{f_l^{(eq)} - f_{\bar{l}}^{(eq)}}{2}, \quad (7b)$$

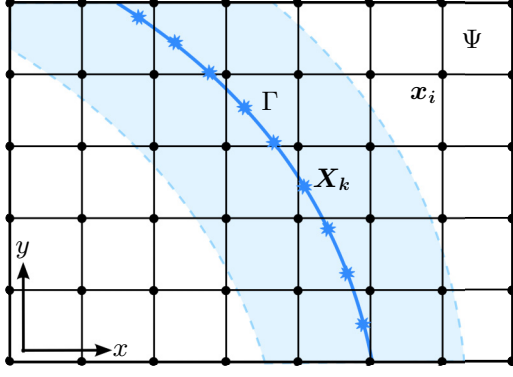


FIG. 1. Schematic view of the IB configuration. A boundary  $\Gamma$  discretized by Lagrangian markers  $\{X_k\}$  is immersed in the fluid domain  $\Psi$  discretized by the lattice nodes  $\{x_i\}$ . The shaded blue area represents the region where the IB forcing is applied, determined by the width of the employed kernel function (16).

where the index  $\bar{l}$  is defined such that  $c_{\bar{l}} = -c_l$ . The collision step is then performed by relaxing symmetric and antisymmetric parts separately,

$$\Omega_l^{TRT} = -\frac{1}{\tau}(f_l^+ - f_l^{(eq)+}) - \frac{1}{\hat{\tau}}(f_l^- - f_l^{(eq)-}), \quad (8)$$

where  $\tau$  remains the relaxation time related to the fluid viscosity, and  $\hat{\tau}$  is an additional relaxation time that does not relate directly to macroscopic quantities and can thus be varied as a numerical parameter. In practice,  $\hat{\tau}$  is often set through the parameter  $\Lambda$  relating both relaxations times [12],

$$\Lambda = \left(\tau - \frac{1}{2}\right) \left(\hat{\tau} - \frac{1}{2}\right). \quad (9)$$

The value of  $\Lambda$  impacts the accuracy and stability properties of the simulations. Optimal values of  $\Lambda$  typically lay between 0.05 and 0.5, as reported in Ref. [2]. In the following, it is set to 1/6.

### B. Immersed-boundary method

The principle of the IB method is schematized in Fig. 1. The no-slip condition on the solid boundaries is enforced through a body force  $\mathbf{g}$  applied on the neighboring lattice nodes. The forcing is introduced in the lattice-Boltzmann method following the scheme of Guo *et al.* [27], as commonly done in prior works [21,22,28]. The TRT collision operator becomes

$$\begin{aligned} \Omega_l^{TRT} = & -\frac{1}{\tau}(f_l^+ - f_l^{(eq)+}) - \frac{1}{\hat{\tau}}(f_l^- - f_l^{(eq)-}) \\ & + \left(1 - \frac{1}{2\tau}\right) S_l^+ + \left(1 - \frac{1}{2\hat{\tau}}\right) S_l^-, \end{aligned} \quad (10)$$

where  $S_l^+ = (S_l + S_{\bar{l}})/2$  and  $S_l^- = (S_l - S_{\bar{l}})/2$  are source terms associated with symmetric and antisymmetric distributions, and

$$S_l = w_l \left[ \frac{c_l \cdot \mathbf{u}}{c_s^2} + \frac{(c_l \cdot \mathbf{u}) \cdot c_l}{c_s^4} \right] \cdot \mathbf{g}. \quad (11)$$

The modification of the collision operator is accompanied by a correction of the flow momentum, namely,

$$\rho \mathbf{u} = \sum_{l=0}^8 f_l \mathbf{c}_l + \frac{1}{2} \mathbf{g}, \quad \rho = \sum_{l=0}^8 f_l. \quad (12)$$

The flow velocity in the absence of momentum correction is denoted by  $\mathbf{u}^\dagger$ , i.e.,  $\rho \mathbf{u}^\dagger = \sum f_l \mathbf{c}_l$ .

The computation of the body force  $\mathbf{g}$  is based on a correction of the flow momentum interpolated on the solid boundary. The boundary is described by a set of Lagrangian markers  $\{X_k\} = \{(X_k, Y_k)\}$ , as indicated in Fig. 1. The lattice nodes, on the other hand, are denoted by  $\{x_i\} = \{(x_i, y_i)\}$ . Based on expression (12), the relation between the body force  $\mathbf{G}$  and the prescribed wall velocity  $\mathbf{U}$  on a boundary marker  $X_k$  is expressed as

$$\mathcal{I}[\rho](X_k) \mathbf{U}(X_k) = \mathcal{I}[\rho \mathbf{u}^\dagger](X_k) + \frac{1}{2} \mathbf{G}(X_k), \quad (13)$$

where  $\mathcal{I}$  denotes the interpolation operator. The momentum correction thus writes

$$\mathbf{G} = 2(\mathcal{I}[\rho] \mathbf{U} - \mathcal{I}[\rho \mathbf{u}^\dagger]). \quad (14)$$

The interpolation of a physical quantity  $\phi$  is performed using a discrete Dirac function  $\delta$ , namely,

$$\mathcal{I}[\phi](X_k) = \sum_{x_i \in \Psi} \phi(x_i) \delta(x_i - X_k) \Delta S_i, \quad (15)$$

where  $\Psi$  denotes the fluid domain, and  $\Delta S_i = \Delta x \Delta y = 1$  is the cell surface. The kernel function is expressed as  $\hat{\delta}(\mathbf{x}) = \hat{\delta}(x) \hat{\delta}(y)$ , with [22]

$$\hat{\delta}(r) = \begin{cases} \frac{1}{2d} [1 + \cos(\frac{\pi r}{d})], & |r| \leq d \\ 0, & |r| > d \end{cases}, \quad (16)$$

and  $d$  the radius of the kernel function, set to 3/2 in the following. This kernel function (16) is chosen for its simplicity, facilitating the integral computation in Sec. III C. More sophisticated kernel functions may, however, be employed in specific IB methods (some examples are given in Appendix B), but this choice does not affect the results presented hereafter.

At each time step, the body force on the immersed boundary is computed on the basis of expression (14). The force is then spread to the lattice nodes, using the same kernel function as that employed for the interpolation. The spread force on a lattice node  $x_i$  writes

$$\mathbf{g}(x_i) = \mathcal{S}[\mathbf{G}](x_i) = \sum_{X_k \in \Gamma} \mathbf{G}(X_k) \delta(x_i - X_k) \Delta S_k, \quad (17)$$

where  $\mathcal{S}$  is the spreading operator,  $\Gamma$  denotes the immersed boundary, and  $\Delta S_k$  is a local surface element; it is generally expressed as  $\Delta S_k = \Delta l_k \epsilon$ , with  $\Delta l_k$  the local distance between two neighboring boundary markers and  $\epsilon$  a boundary width usually set to unity—as done in the present work—or in some cases computed explicitly [23].

### III. ANALYSIS AND CORRECTION OF THE VISCOSITY DEPENDENCE

The effect of the fluid viscosity on the macroscopic solution is analyzed in the following. The general scaling laws that must be verified by the macroscopic solution are first introduced in Sec. III A. The above-described IB method is not able to reproduce these scaling properties, as discussed in Sec. III B. This analysis leads to a correction of the IB force that is derived in Sec. III C.

#### A. Macroscopic scaling laws

Generally, a lattice-Boltzmann problem involves at least two nondimensional physical parameters, the Reynolds and Mach numbers,

$$\text{Re} = \frac{U_r D}{\nu}, \quad \text{Ma} = \frac{U_r}{c_s}, \quad (18)$$

where  $U_r$  and  $D$  are the reference velocity and reference length of the problem, respectively,  $\nu = c_s^2(\tau - 1/2)$  is the kinematic viscosity of the fluid, and  $c_s$  is the sound speed. Numerical simulations are usually performed in the limit  $\text{Ma} \ll 1$ . Under this condition, it is expected that variations of  $\text{Ma}$  do not impact the numerical solution,  $\text{Re}$  remaining the only relevant physical parameter. However,  $\text{Ma}$  is often varied as a numerical parameter, through variations of the reference velocity  $U_r$ , which alters the nondimensional physical time step and thus the cost of the computation. If the Reynolds number is kept constant, variations of  $U_r$  are necessarily associated with variations of the relaxation time  $\tau$ . In order to be physically consistent, the numerical solution should thus be independent of  $\tau$ , so that it depends only on  $\text{Re}$ . This aspect is addressed in the following.

In any physical configuration, the flow solution can be described by a set of nondimensional physical quantities, as the nondimensional pressure and velocity,

$$\mathbf{u}^* = \frac{\mathbf{u}}{U_r}, \quad P^* = \frac{P - P_r}{\rho_r U_r^2}, \quad (19)$$

where  $U_r$ ,  $\rho_r$ , and  $P_r$  are the reference velocity, density, and pressure of the considered problem. In a lattice-Boltzmann framework, the density  $\rho$  and pressure  $P$  are connected by the state equation, namely,  $P = \rho c_s^2$ . The second equation of (19) may thus be replaced by a density equation,

$$\rho^* = \frac{\rho - \rho_r}{\rho_r U_r^2}. \quad (20)$$

In addition, a complete description of an IB problem also involves the nondimensional IB force,

$$\mathbf{g}^* = \frac{\mathbf{g}D}{\rho_r U_r^2}. \quad (21)$$

In the following, two sets of dimensional quantities, solutions of two distinct computations, are considered:  $(\rho_1, \mathbf{u}_1, \mathbf{g}_1)$  and  $(\rho_2, \mathbf{u}_2, \mathbf{g}_2)$ . Both sets are associated with the same reference density  $\rho_r$  and length  $D$ . However, the reference velocity differs from one case to the other; these velocities, denoted by  $U_{r,1}$  and  $U_{r,2}$ , are connected by the scaling factor defined as  $\lambda = U_{r,2}/U_{r,1}$ . Moreover, it is assumed that sets 1 and 2 result in the same set of nondimensional quantities,  $(\rho^*_1 =$

$\rho^*_2, \mathbf{u}^*_1 = \mathbf{u}^*_2, \mathbf{g}^*_1 = \mathbf{g}^*_2)$ ; i.e., they are both solutions of the same physical problem. In particular, the Reynolds number is the same in both cases. As a result,  $\lambda$  also designates the viscosity ratio between configurations 1 and 2,  $\lambda = \nu_2/\nu_1$ ; in a lattice-Boltzmann framework,  $\lambda$  thus connects the relaxation times employed in both computations,  $\lambda = (\tau_2 - 1/2)/(\tau_1 - 1/2)$ . In order to verify the above-described scaling laws (19)–(21), the dimensional quantities should verify

$$\mathbf{u}_1 = \frac{1}{\lambda} \mathbf{u}_2, \quad \rho_1 = \left(1 - \frac{1}{\lambda^2}\right) \rho_r + \frac{1}{\lambda^2} \rho_2, \quad \mathbf{g}_1 = \frac{1}{\lambda^2} \mathbf{g}_2. \quad (22)$$

It is assumed that the Mach number is small enough so that density variations can be neglected, i.e.,  $\rho_1 \approx \rho_2 \approx \rho_r$ , as it is generally verified in lattice-Boltzmann simulations. Using expression (12), the IB forces can be rewritten as  $\mathbf{g}_1 = 2\rho_r(\mathbf{u}_1 - \mathbf{u}_1^\dagger)$  and  $\mathbf{g}_2 = 2\rho_r(\mathbf{u}_2 - \mathbf{u}_2^\dagger)$ . This results in the following scaling of the noncorrected velocities:

$$\mathbf{u}_1^\dagger = \left(\frac{1}{\lambda} - \frac{1}{\lambda^2}\right) \mathbf{u}_2 + \frac{1}{\lambda^2} \mathbf{u}_2^\dagger. \quad (23)$$

While the physical quantities exhibit self-similar scaling properties (22), expression (23) emphasizes that the numerical quantity  $\mathbf{u}^\dagger$  cannot be directly rescaled using  $\lambda$ , since  $\mathbf{u}_1^\dagger$  depends not only on  $\mathbf{u}_2^\dagger$  but also on  $\mathbf{u}_2$ . This property will lead to the numerical error analyzed hereafter.

#### B. Immersed-boundary viscosity error

The scaling of the IB force, previously expressed on the lattice nodes (22), must also be verified on the boundary markers, i.e.,  $\mathbf{G}_2 = \lambda^2 \mathbf{G}_1$ . If  $\mathbf{G}_1$  is computed on the basis of expression (14), this scaling relation becomes

$$\mathbf{G}_2 = 2\rho_r \lambda^2 (\mathbf{U}_1 - \mathcal{I}[\mathbf{u}_1^\dagger]). \quad (24)$$

It should be noted that, following the above-mentioned low-Mach assumption, density variations have been neglected, leading to  $\mathcal{I}[\rho_1] = \rho_r$  and  $\mathcal{I}[\rho_1 \mathbf{u}_1^\dagger] = \rho_r \mathcal{I}[\mathbf{u}_1^\dagger]$ . Using the scaling laws (22) and (23), expression (24) can be rewritten as a function of  $\mathbf{U}_2$ ,  $\mathbf{u}_2$ , and  $\mathbf{u}_2^\dagger$ , namely,

$$\mathbf{G}_2 = 2\rho_r \lambda \mathbf{U}_2 + 2\rho_r (1 - \lambda) \mathcal{I}[\mathbf{u}_2] - 2\rho_r \mathcal{I}[\mathbf{u}_2^\dagger]. \quad (25)$$

Moreover, by definition [expression (12)], the velocity  $\mathbf{u}_2$  on a lattice node verifies

$$\mathbf{u}_2 = \mathbf{u}_2^\dagger + \frac{1}{2\rho_r} \mathcal{S}[\mathbf{G}_2]. \quad (26)$$

Finally, the IB force verifying the scaling properties writes

$$\mathbf{G}_2 = 2\rho_r \lambda (\mathbf{U}_2 - \mathcal{I}[\mathbf{u}_2^\dagger]) + (1 - \lambda) \mathcal{I}[\mathcal{S}(\mathbf{G}_2)]. \quad (27)$$

In the case  $\lambda \neq 1$ , expression (27) reduces to the standard velocity correction (14),  $\mathbf{G}_2 = 2\rho_r (\mathbf{U}_2 - \mathcal{I}[\mathbf{u}_2^\dagger])$ , only if the interpolation and spreading operators verify

$$\mathcal{I}[\mathcal{S}(\phi)] = \phi. \quad (28)$$

However, this condition is generally not verified when employing the explicit approach described in Sec. II B, thus introducing a  $\lambda$ -dependent (i.e.,  $\tau$ -dependent) term in the computation of the momentum correction. As this term is not considered in the standard method, the latter cannot reproduce the scaling properties of the physical solution.

In practice, it is useful to define  $\lambda$  as the ratio between the employed relaxation time  $\tau$  and a reference relaxation time  $\tau_r$ . The reference relaxation time should ensure minimal boundary error, so that expression (27) describes the evolution of the IB error as the relaxation time departs from an optimal value. The accurate optimal value of  $\tau_r$  may vary from one physical configuration to the other. Detailed analysis of the connections between the optimal  $\tau_r$  and the physical and numerical parameters would be beyond the scope of the present paper. However, the results reported by Le and Zhang [24] indicate that the velocity error related to the IB method is minimal for relaxation times close to unity. This is supported by the results of Seta *et al.* [22] and also by the present results detailed in Sec. IV. Therefore, it is assumed here that the optimal value of  $\tau_r$  should remain close to one, and the value  $\tau_r = 1$  is employed in the following. The expression of the

scaling factor then becomes

$$\lambda = 2\tau - 1. \quad (29)$$

Therefore, expression (27) may be seen as a description of the evolution of the IB-force error as the relaxation time departs from unity. A correction of this error is proposed in the following.

### C. Correction of the Immersed-boundary force

A first approach in order to achieve viscosity independence of the momentum correction consists in ensuring the condition (28) through implicit algorithms, as suggested by Seta *et al.* [22]. However, this approach introduces substantial additional computational costs, as discussed in Sec. I. Here an explicit approach is proposed, based on an approximation of the reinterpolated IB force,  $\mathcal{I}[S(\mathbf{G})]$ .

First, a continuous formulation of  $\mathcal{I}[S(\mathbf{G})]$  is considered,

$$\mathcal{I}[S(\mathbf{G})](\mathbf{X}_m) = \iiint_{\mathbf{x}_i \in \Psi} \int_{\mathbf{X}_k \in \Gamma} \mathbf{G}(\mathbf{X}_k) \delta(\mathbf{x}_i - \mathbf{X}_k) \delta(\mathbf{x}_i - \mathbf{X}_m) d\mathbf{X}_k d^2\mathbf{x}_i. \quad (30)$$

Then it is assumed that the curvature of the immersed boundary is small, so that it can be approximated by a straight wall. This simplifies the integral in (30) since  $\mathbf{x}_i$ ,  $\mathbf{X}_m$ , and  $\mathbf{X}_k$  can be decomposed in a frame  $(\mathbf{p}, \mathbf{n})$ , where  $\mathbf{p}$  and  $\mathbf{n}$  are, respectively, parallel and normal to the straight boundary. The resulting decompositions are denoted by  $\mathbf{x} = (p, n)$  (Eulerian frame) or  $\mathbf{X} = (P, N)$  (Lagrangian frame). Consequently, the kernel functions in (30) can be decomposed as  $\delta(\mathbf{x}_i - \mathbf{X}_k) = \hat{\delta}(p_i - P_k) \hat{\delta}(n_i - N_k)$  and  $\delta(\mathbf{x}_i - \mathbf{X}_m) = \hat{\delta}(p_i - P_m) \hat{\delta}(n_i - N_m)$ , and the IB force can be expressed as  $\mathbf{G}(\mathbf{X}_k) = \mathbf{G}(P_k)$ . Recalling that for a straight boundary the normal distance between a given lattice node  $\mathbf{x}_i$  and any boundary marker is constant, namely,  $(n_i - N_k) = (n_i - N_m)$ , expression (30) becomes

$$\mathcal{I}[S(\mathbf{G})](\mathbf{X}_m) \approx \iint_{\mathbf{x}_i \in \Psi} \hat{\delta}(p_i - P_m) \hat{\delta}(n_i - N_m)^2 \left[ \int_{\mathbf{X}_k \in \Gamma} \mathbf{G}(P_k) \hat{\delta}(p_i - P_k) dP_k \right] dn_i dp_i. \quad (31)$$

The momentum correction is then linearized in the vicinity of  $\mathbf{X}_m$ , in the form

$$\mathbf{G}(P_k) = \mathbf{G}(P_m) + (P_k - P_m) \frac{\partial \mathbf{G}}{\partial P}(P_m). \quad (32)$$

After some straightforward developments detailed in Appendix A, and especially using identities  $\int \hat{\delta}(x) dx = 1$  and  $\int x \hat{\delta}(x) dx = 0$ , expression (31) eventually reduces to

$$\mathcal{I}[S(\mathbf{G})](\mathbf{X}_m) \approx \mathbf{G}(\mathbf{X}_m) \int \hat{\delta}(r)^2 dr. \quad (33)$$

This allows us to express the reinterpolated IB force as

$$\mathcal{I}[S(\mathbf{G})] \approx \kappa \mathbf{G}, \quad (34)$$

where  $\kappa = \int \hat{\delta}(r)^2 dr$  is an error factor that depends on the employed kernel function. In the case of the kernel function employed in this work (16),  $\kappa$  is equal to  $3/(4d)$ , i.e.,  $\kappa = 1/2$  using  $d = 3/2$ . The values of  $\kappa$  for other commonly used kernel functions are given in Appendix B.

The approximated term  $\mathcal{I}[S(\mathbf{G})]$  can be introduced in expression (27). Finally, the IB force can be rewritten as

$$\mathbf{G} = \frac{\lambda}{1 + \kappa(\lambda - 1)} 2\rho_r [\mathbf{U} - \mathcal{I}(\mathbf{u}^\dagger)]. \quad (35)$$

Expression (35) is the viscosity-independent IB scheme proposed in this work. As it is a straightforward correction of the standard IB method, it does not involve any additional implementation effort or computational cost. Moreover, the corrected method reduces to the standard one when  $\tau = 1$ , as  $\lambda$  is equal to one in this case. As a result, the good properties of the IB method when  $\tau$  is close to one (accuracy, stability, robustness) are conserved; the method is only corrected when the relaxation time departs from unity. Its accuracy is analyzed and compared to that of the noncorrected IB method in Sec. IV.

Even though the above analysis has been performed in a two-dimensional framework for sake of brevity and clarity, it should be mentioned that its extension to three-dimensional configurations is straightforward. Indeed, a three-dimensional version of expression (30) can be computed similarly through a plane-wall approximation and a two-dimensional linearization of the IB force on the boundary. This development and the associated validation tests are, however, left for future works.

## IV. NUMERICAL RESULTS

The accuracy of the proposed IB method is analyzed in this section on the basis of several test cases. First, a summary of

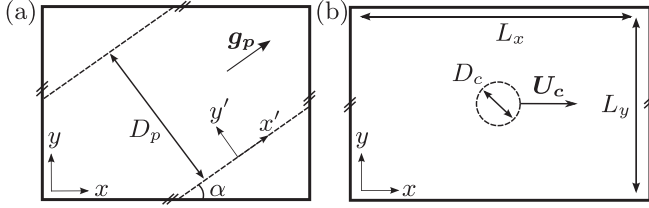


FIG. 2. Sketch of the physical configurations: (a) the inclined Poiseuille flow and (b) the circular cylinder towed in a periodic channel. Solid lines represent the boundaries of the computational domain, and dashed lines indicate the immersed boundaries.

the implemented algorithm and a description of the considered physical configurations is proposed in Sec. IV A. The first configuration is the Poiseuille flow; the related computational results are commented in Sec. IV B. Then the flow around a cylinder towed in still fluid is considered in Sec. IV C. Finally, the behavior of the method is investigated in the case of a cylinder oscillating in still fluid in Sec. IV D.

### A. Algorithm and physical setup

In the following, results issued from the noncorrected and corrected IB methods are considered. In both cases, the implemented algorithms can be summarized as follows, the methods differing only at step 6:

- (1) Distribution functions  $\{f_i\}$  and the macroscopic quantities are known at the beginning of a time step
- (2) TRT collision is performed (6)–(8)
- (3) Postcollision distributions are streamed (4)
- (4) Position and velocity of the IB markers are updated
- (5) Interpolation of the noncorrected flow momentum on boundary markers (15)
- (6) Computation of the IB force (35) with (i)  $\lambda = 1$  (noncorrected method) or (ii)  $\lambda = 2\tau - 1$  (29) and  $\kappa = 1/2$  (corrected method)
- (7) Spreading of the momentum correction (17)
- (8) Update of the macroscopic quantities (12)

This algorithm is applied to three physical configurations, schematized in Fig. 2. The first case is an inclined Poiseuille flow. Parallel and inclined immersed boundaries are placed in a periodic computational domain. The distance between both walls is called  $D_p$ . The angle between the walls and the  $x$  axis is denoted by  $\alpha$ ; it is set to  $30^\circ$  in the following. The flow is driven by the body force  $\mathbf{g}_p$  parallel to the walls. Based on the characteristic velocity  $U_{r,p} = \sqrt{g_p D_p}$ , the Reynolds number is defined as

$$\text{Re}_p = \frac{\sqrt{g_p D_p} D_p}{\nu}. \quad (36)$$

A new frame  $(x', y')$  is introduced; it is attached to the lower wall, and the  $x'$  axis is parallel to the flow direction. In this frame, the analytical flow solution is

$$\frac{u_{x'}(y')}{U_{r,p}} = \frac{1}{2} \text{Re} \frac{y'}{D_p} \left( 1 - \frac{y'}{D_p} \right), \quad (37)$$

where  $u_{x'}$  is the fluid velocity in the  $x'$  direction.

The second configuration is a circular cylinder of diameter  $D_c$  immersed in a  $x$ -periodic channel and moving at velocity

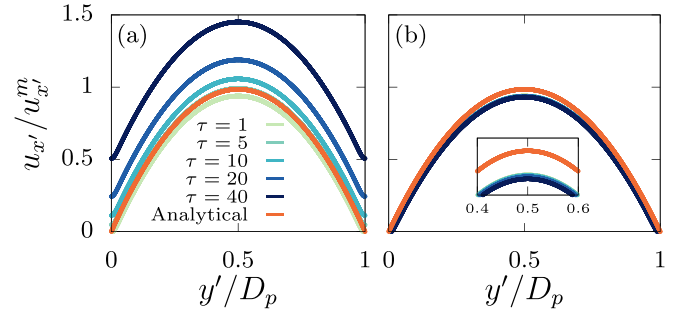


FIG. 3. Effect of the relaxation time on the Poiseuille flow solution: (a) standard IBM and (b) corrected IBM.  $\text{Re}_p = 0.1$  and  $D_p = 50\Delta n$ .

$U_c$  in the  $x$  direction. The dimensions of the computational domain are set by the lengths  $L_x$  and  $L_y$ , as indicated in Fig. 2(b). No-slip boundary conditions are set on the upper and lower boundaries of the computational domain, using the bounce-back method [2]. Two cases are considered: the cylinder towed at a constant velocity  $U_c$ , and the cylinder oscillating in still fluid. In the latter case, the cylinder exhibits a sinusoidal motion described by  $x_c(t) = A_c \sin(2\pi f_c t)$ , where  $x_c(t)$  is the  $x$  position of the cylinder at time  $t$ , and  $A_c$  and  $f_c$  are the motion amplitude and frequency. In both cases, the Reynolds number is defined as

$$\text{Re}_c = \frac{U_{r,c} D_c}{\nu}, \quad (38)$$

where  $U_{r,c}$  is the typical flow velocity, equal to  $|U_c|$  in the towed-cylinder case, and to  $2\pi A_c f_c$  in the oscillating-cylinder case. The drag coefficient is used to analyze the fluid forces exerted on the body; it is defined as  $C_x = 2F_x / \rho_r U_{r,c}^2 D_c$ , where  $F_x$  is the sectional fluid force in the  $x$  direction, computed by summing the IB momentum corrections on the immersed boundary, namely,

$$F_x = \sum_{X_k \in \Gamma} \mathbf{G}(X_k) \cdot \mathbf{e}_x \Delta S_k. \quad (39)$$

The numerical solutions obtained for these physical configurations and issued from the standard (Sec. II B) and corrected (Sec. III C) IB methods are analyzed hereafter. As the accuracy of the standard IB method has widely been studied in prior works [28], this aspect is not directly addressed in the following. In contrast, the focus is placed on the comparison between the standard and corrected IB methods, especially concerning the effect of the relaxation time. Additional validation results on the flow past a cylinder immersed in a current are provided in Appendix C.

### B. Poiseuille flow

The numerical solutions for the Poiseuille flow are studied hereafter. The Reynolds number (36) is set to  $\text{Re}_p = 0.1$ , and the width of the channel is  $D_p = 50\Delta n$ . Figure 3 shows the evolution of the  $x'$  velocity as a function of  $y'$ , issued from both methods and for different values of the relaxation time. In this figure, the flow velocity is normalized by the maximum analytical velocity, namely,  $u_{x'}^m = U_{r,p} \text{Re}/8$ . For  $\tau = 1$ , the numerical solution issued from the standard IB method is

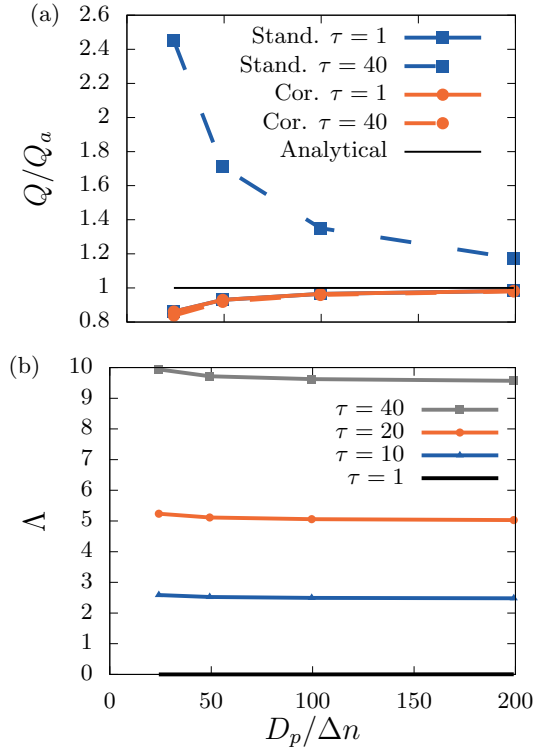


FIG. 4. Effect of the grid resolution on the Poiseuille flow solution: (a) evolution of the flow rate  $Q$  issued from the standard and corrected IB methods, for  $\tau = 1$  and  $\tau = 40$ , as a function of  $D_p/\Delta n$ ; (b) evolution of  $\Lambda$ , the relative difference between the flow rate errors of both methods, for different values of the relaxation time, as a function of  $D_p/\Delta n$ .

close to the analytical solution. In particular, the wall velocity is close to zero, and no clear boundary slip is noted.

The numerical solution substantially departs from the analytical one as the relaxation time increases. This is the boundary slip error that has been described in prior works [22,24]. This error is expected from the analysis performed in Sec. III: the standard IB method does not take into account the  $\tau$ -dependent term in the computation of the IB forcing, resulting in a  $\tau$ -dependent numerical solution. In contrast, the impact of the relaxation time on the flow solution is very small when using the present corrected IB method [Fig. 3(b)], supporting the relevancy of the approach described in Sec. III C. Overall, the flow solution remains close to that obtained with  $\tau = 1$ , which by definition is identical for both methods.

The simulated flow tends to the exact solution as the mesh size increases. This is illustrated in Fig. 4(a), on the basis of the flow rate  $Q = \int u_x dy'$ . In the figure,  $Q$  is normalized by the analytical flow rate,  $Q_a = U_{r,p} D_p \text{Re} / 12$ . Moreover, the grid resolution is varied together with the Reynolds number, which ranges from 0.05 to 0.4, so that the relaxation time and the reference velocity are kept constant. The convergence of the flow solution is well noted for both the noncorrected and corrected methods and for the two considered relaxation times,  $\tau = 1$  and 40. Among the four considered cases, three of them exhibit very similar flow rate values. Indeed, the standard and corrected methods are expected to be equivalent for  $\tau = 1$ . In addition, the corrected method is expected to be

almost unaffected by variations of  $\tau$ , so the flow rates for  $\tau = 1$  and  $\tau = 40$  are very close. In contrast, the flow rates issued from the noncorrected method for  $\tau = 40$  greatly depart from those previously described. For a given grid resolution, the absolute error on the predicted flow rate,  $E = Q - Q_a$ , is greatly increased in this case. Even though this error tends to decrease as the mesh size increases, it remains significant for high grid resolutions, as shown by the case  $D_p = 200\Delta n$ . Despite the apparent convergence of the flow rates predicted by the corrected and noncorrected methods, denoted by  $Q_c$  and  $Q_{nc}$ , the relative effect of the IB-forcing correction remains constant for any grid resolution. This is quantified through the relative difference between errors issued from both methods, namely,

$$\Lambda = \left| \frac{E_{nc} - E_c}{E_c} \right| = \left| \frac{Q_{nc} - Q_c}{Q_c - Q_a} \right|, \quad (40)$$

where  $E_{nc} = Q_{nc} - Q_a$  and  $E_c = Q_c - Q_a$ . The evolution of  $\Lambda$  as a function of the grid resolution is depicted in Fig. 4(b), for various values of the relaxation time. As expected, the effect of the correction increases as a function of  $\tau$ . Moreover,  $\Lambda$  remains close to constant as a function of  $D_p/\Delta n$ , indicating that the relative variation of the numerical error between the noncorrected and corrected solvers is constant. This is in agreement with the analysis performed in Sec. III, since the magnitude of the correction in Eq. (35) is mesh-independent. This confirms that the proposed correction remains beneficial for any grid resolution.

The low sensitivity of the flow solution with respect to the relaxation time, using the proposed correction, is expected in the Poiseuille flow case since this configuration is fully consistent with the assumptions made in Sec. III C. Indeed, the immersed boundary exhibits a straight geometry, and the momentum correction on the boundary is expected to be close to uniform since the flow is uniform in the  $x'$  direction. In order to analyze the accuracy of the method on a more general geometry, the flow past a circular cylinder is considered hereafter.

### C. Flow around a cylinder towed in still fluid, $\text{Re}_c = 0.01$

The flow around a cylinder towed at a constant velocity in a periodic channel is considered in the following. The Reynolds number is set to  $\text{Re}_c = 0.01$ , and the cylinder diameter is  $D_c = 10\Delta n$ . The dimensions of the computational domain are set to  $L_x = L_y = 16D_c$ . After a transient period, the flow reaches a steady state. The resulting drag force  $C_x$  exerted on the cylinder is plotted in Fig. 5, for different values of the relaxation time. In this plot the drag force is normalized by the reference drag force  $C_{x,r}$ , chosen as the drag force issued from the case  $\tau = 1$ . In order to keep the Reynolds number constant, the relaxation time is varied together with the typical flow velocity (i.e., velocity of the towed cylinder); the latter varies from  $|U_c| = 1.67 \times 10^{-4}$  to  $|U_c| = 1.65 \times 10^{-2}$  over the considered range of  $\tau$ . In the case of the standard IB method, the computed drag force monotonically decreases as a function of the relaxation time, leading to a substantial relative error for  $\tau = 50$ , of approximately 30% compared to the reference drag. In contrast, the drag force issued from the corrected IB method remains close to constant as a



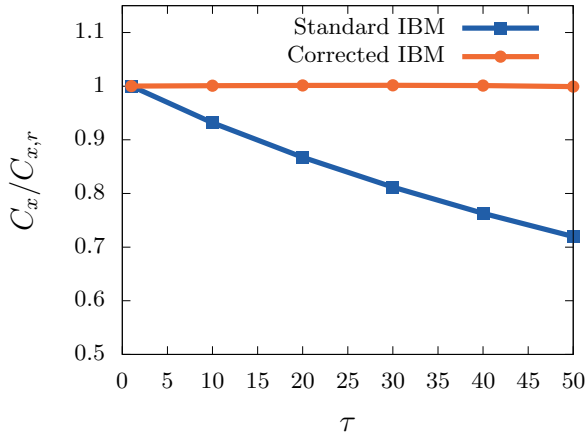


FIG. 5. Effect of the relaxation time on the drag force on a cylinder towed in a periodic channel, at  $Re_c = 0.01$ , for the non-corrected and corrected IB methods. The cylinder diameter is set to  $D_c = 10\Delta n$ .

function of  $\tau$ . This supports that the proposed approach remains consistent for curved geometries, despite the straight-wall approximation made in Sec. III C. It should be noted that the apparent curvature of the immersed boundary relates to the mesh resolution. In the present case, a relatively coarse mesh resolution is employed, namely,  $D_c = 10\Delta n$ , corresponding to a high boundary curvature. A finer mesh resolution would result in a lower apparent curvature of the boundary, thus increasing the validity of the straight-wall assumption.

In the absence of correction, the alteration of the drag force as the relaxation time increases (see Fig. 5) is associated with a major alteration of the flow in the vicinity of the body. This is illustrated in Fig. 6, which shows the streamlines around the cylinder predicted by the standard and corrected IB methods, for  $\tau = 1$  and  $\tau = 30$ . In the first case, streamlines issued from both methods are identical. Qualitatively, the streamlines are consistent with the expected flow solution. In particular, the fluid appears to flow around the cylinder, and no fluid penetration is observed through the immersed boundary. However, an important flow penetration is noted when the relaxation time is increased to  $\tau = 30$ . This error is similar to the boundary slip previously observed in the case of the Poiseuille flow: for large relaxation times, the method fails in imposing the wall velocity in the vicinity of the immersed boundary. The resulting decrease of the wall stresses is expected to be accompanied by a substantial decrease of the drag force on the cylinder, as already confirmed in Fig. 5. This defect is well corrected by the present method. Indeed, no flow penetration is noted on the solution issued from the corrected method, whose streamlines are close to that associated with the reference case  $\tau = 1$ .

**D. Flow around a cylinder oscillating in still fluid,  $Re_c = 3$**

In Sec. IV C, the IB method has been analyzed for a low value of the Reynolds number  $Re_c$ , associated with large values of the relaxation time  $\tau$ . In the following, the focus is placed on relaxation times lower than unity. Moreover, an unsteady configuration is considered, namely, the flow past

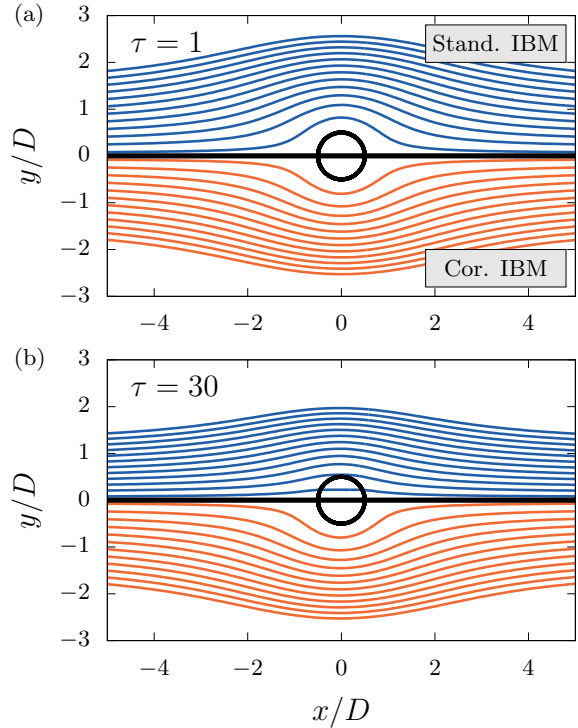


FIG. 6. Effect of the relaxation time on the streamlines around a cylinder towed in a periodic channel, at  $Re_c = 0.01$ , for the standard and corrected IB methods: (a)  $\tau = 1$  and (b)  $\tau = 30$ . The cylinder diameter is set to  $D_c = 10\Delta n$ . The streamlines are plotted in the frame attached to the cylinder axis, and the relative flow is from left to right.

an oscillating cylinder. The Reynolds number based on the peak displacement velocity (see Sec. IV A) is set to 3, and the amplitude of the oscillations is  $A_c = D_c/2$ . The cylinder diameter and the computational-domain dimensions remain unchanged, i.e.,  $D_c = 10\Delta n$  and  $L_x = L_y = 16D_c$ .

The sinusoidal motion of the cylinder is accompanied by an oscillating drag force exerted on the body, as depicted in Fig. 7(a). In this figure, the numerical solution is issued from the noncorrected IB method for  $\tau = 1$ . The force signal is sinusoidal, and its frequency is equal to the displacement frequency. The associated flow pattern is visualized in Fig. 7(b), which shows isocontours of the vorticity  $\omega = \partial u_x/\partial y - \partial u_y/\partial x$  at two different instants.

The effect of the relaxation time on the drag force is investigated in Fig. 8. First, selected time histories of  $C_x$  are shown in Fig. 8(a), for three different values of  $\tau \leq 1$ . While the solution issued from the corrected IB method is hardly altered by variations of the relaxation time, a substantial effect of  $\tau$  is noted in the case of the standard IB method. Indeed, the time history of  $C_x$  for  $\tau = 0.5001$  exhibits high-frequency fluctuations that are not present in the case  $\tau = 1$ . In addition, this effect seems to be accompanied by a slight increase of the amplitude of the low-frequency component of the drag-force signal. In order to quantify the amplitude of these spurious oscillations, the drag-force signals have been high-pass filtered, using a Butterworth filter with a cutoff frequency equal to  $4f_c$  (it is recalled that  $f_c$  is the body motion frequency). The root-mean-square (RMS) of the resulting high-pass filtered force

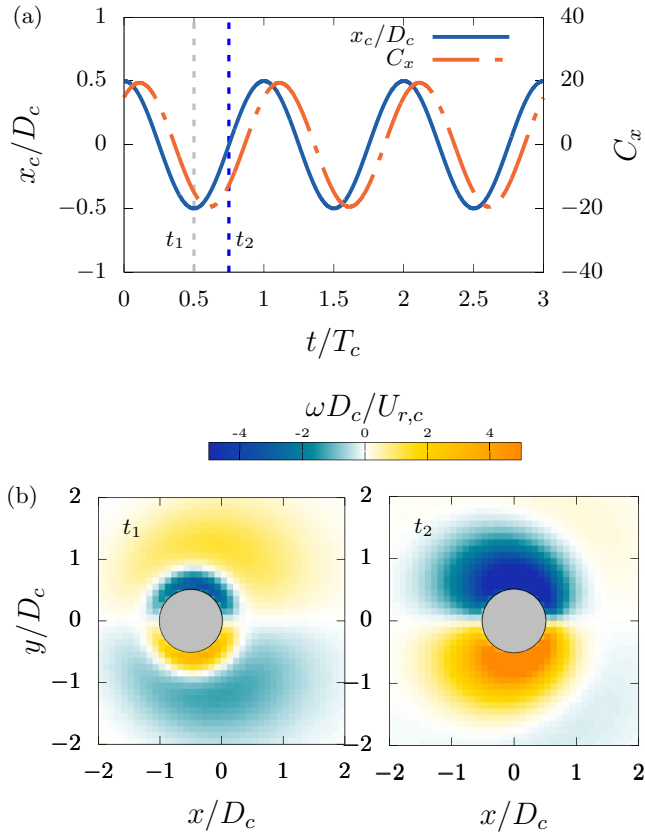


FIG. 7. Flow past a cylinder oscillating in still fluid at  $Re_c = 3$ , simulated using the noncorrected IB method for  $\tau = 1$ : (a) selected time history of the body displacement  $x_c$  and drag coefficient  $C_x$ , and (b) and isocontours of the nondimensional vorticity at two different instants  $t_1$  and  $t_2$ , indicated by vertical dashed lines in (a). The diameter of the cylinder is  $D_c = 10\Delta n$ .

signals is plotted in Fig. 8(b) as functions of the relaxation time. For both methods, the spurious oscillations remain small in the range  $\tau \in [0.6, 1]$ . However, for values lower than 0.6, their amplitude rapidly increases as the relaxation time decreases, when using the noncorrected IB method. This error is well corrected by the present method: the spurious-oscillation amplitude for  $\tau = 0.5001$  is very close to that observed for  $\tau = 1$ .

The lattice-Boltzmann method is often expected to become less stable for low relaxation times. In the present case, the oscillations observed in Fig. 8 can be analyzed on the basis of the corrected IB-forcing scheme (35). When  $\tau < 1$ , the correction tends to decrease the magnitude of the IB forcing. As shown in Fig. 8(a), this decrease does not affect the low-frequency evolution of the fluid forces, but it results in the damping of the high-frequency fluctuations. Similarly, these high-frequency fluctuations, in the absence of correction, may thus be attributed to an excessively strong IB forcing, i.e., a too stiff forcing of the flow close to the immersed boundary.

The present correction method is based on the approximation of the reinterpolated IB force,  $\mathcal{I}[S(\mathbf{G})] \approx \kappa \mathbf{G}$ , as described by expression (34). This assumption is examined in Fig. 9, which shows the evolution of  $\mathcal{I}[S(G_x)]$  and  $\kappa G_x$

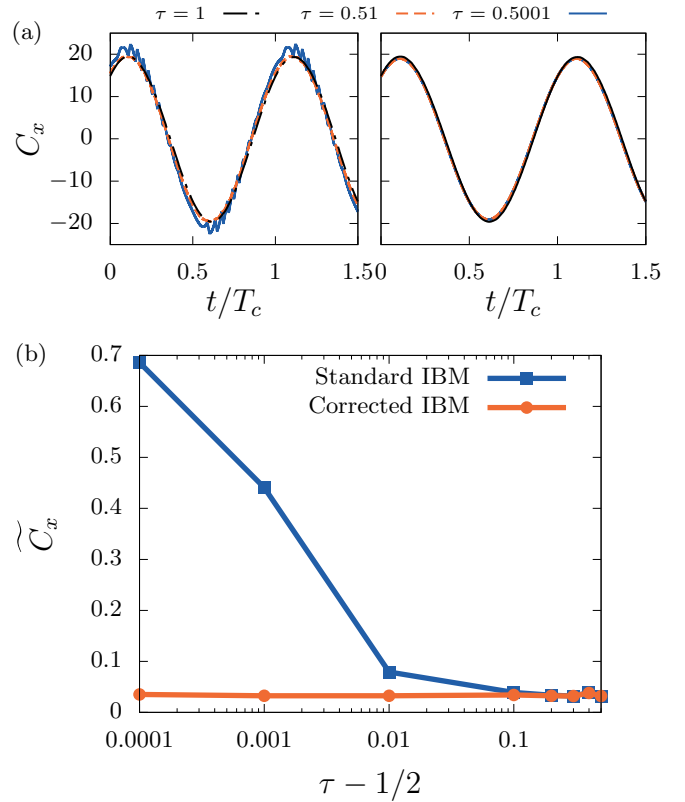


FIG. 8. Effect of the relaxation time on the drag force exerted on a cylinder oscillating in still fluid, at  $Re_c = 3$ , for the noncorrected and corrected IB methods: (a) selected time histories of the drag coefficient and (b) evolution of the RMS of the high-pass filtered drag force  $\tilde{C}_x$  as a function of the relaxation time.

on the immersed boundary at different phases of the body-motion period, where  $G_x$  is the IB force in the  $x$  direction, i.e., the direction of body motion. The values of  $\mathcal{I}[S(G_x)]$  are determined by implementing an additional routine that reinterpolates the IB force after the spreading step (step 7 in the algorithm described in Sec. IV A). The figure emphasizes the variability of  $\mathcal{I}[S(G_x)]$ , as it exhibits important variations

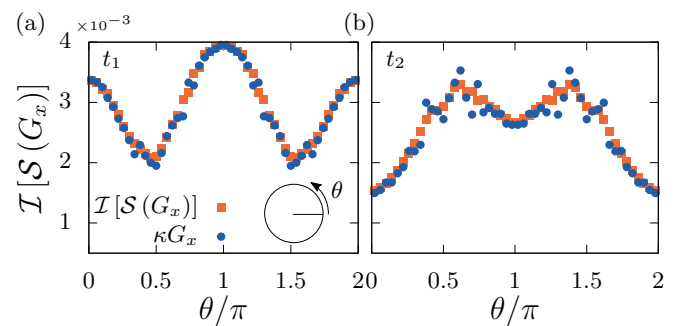


FIG. 9. Examination of approximation (34), for the oscillating-cylinder case: evolution of the reinterpolated momentum correction in the  $x$  direction  $\mathcal{I}[S(G_x)]$  on the immersed boundary as a function of the polar angle  $\theta$ , at times (a)  $t_1$  and (b)  $t_2$  indicated in Fig. 7(a), and comparison with the approximation  $\kappa G_x$ . The data are issued from the same simulation as in Fig. 7.

along the cylinder surface and also strongly differs from one instant to the other. Despite this variability, the approximation  $\kappa G_x$  appears to be generally close to the reinterpolated force, even though small discrepancies are noted locally, especially at time  $t_2$  [Fig. 9(b)]. The reasonable validity of the approximation (34) corroborates the above results and supports the relevancy of the present method.

## V. SUMMARY

In this work, the viscosity error of the standard IB method has been analyzed, and a viscosity-dependent correction has been proposed. The proposed method is straightforward and does not involve any additional implementation effort or computational time. The validity of the method has been examined for several physical configurations involving steady and unsteady shear flows. The viscosity independence of the solver is achieved over a large range of investigated relaxation times, from  $\tau = 0.5001$  to  $\tau = 50$ . For  $\tau > 1$ , the previously reported boundary-slip error is well corrected. In the case of the flow around a cylinder towed in a channel, this allows us to avoid flow penetration and related errors on the computed drag force exerted on the body. For  $\tau < 1$ , the present method suppresses the spurious oscillations emerging when using the standard method.

This correction of the viscosity error of the lattice-Boltzmann IB method may substantially extend the range of application of the method. Indeed, using the noncorrected method, the boundary-slip error tends to drastically limit the possible range of relaxation times employed in the simulations. In particular, high values of  $\tau$  are generally prohibited, making this method hardly suitable for the simulations of low Reynolds number flows. In contrast, the corrected method proposed in this work may provide an accurate and efficient tool for the simulation of such flows. Moreover, the present method may be relevant for the simulation of flows involving complex fluids with varying viscosities, since these configurations require a viscosity-independent accuracy which is generally difficult to achieve with lattice-Boltzmann methods.

$$\mathcal{I}[\mathcal{S}(\mathbf{G})](\mathbf{X}_m) = \mathbf{G}(P_m) \int \hat{\delta}(p_i - P_m) dp_i \int \hat{\delta}(n_i - N_m)^2 dn_i + \frac{\partial \mathbf{G}}{\partial P}(P_m) \int (p_i - P_m) \hat{\delta}(p_i - P_m) dp_i \int (n_i - N_m)^2 dn_i. \quad (\text{A5})$$

Using variables  $r' = n_i - N_m$  and  $r'' = p_i - P_m$  and the above-mentioned identities, this reduces to

$$\mathcal{I}[\mathcal{S}(\mathbf{G})](\mathbf{X}_m) = \mathbf{G}(\mathbf{X}_m) \int \hat{\delta}(r')^2 dr', \quad (\text{A6})$$

which corresponds to expression (33).

## APPENDIX B: MOMENTUM CORRECTION FOR VARIOUS KERNEL FUNCTIONS

As described by expressions (34), (35), and (33), the IB-forcing correction proposed in this work is based on the computation of  $\kappa = \int \hat{\delta}(r)^2 dr$ . Thus, the correction can be computed analytically for any kernel function  $\hat{\delta}$ . In the present work, the correction associated with the employed kernel function (16) is  $\kappa = \frac{3}{4d}$ .

## ACKNOWLEDGMENTS

The project MACBION leading to this publication has received funding from Excellence Initiative of Aix-Marseille University—A\*MIDEX, a French Investissements d'Avenir programme, the LABEX MEC, and the SINUMER project (ANR-18-CE45-0009-01) of the French National Research Agency (ANR).

## APPENDIX A: DETAILS ON THE COMPUTATION OF THE IB-FORCE CORRECTION

The integral into brackets in (31) is denoted by  $A$  in the following, namely,

$$A = \int_{\mathbf{X}_k \in \Gamma} \mathbf{G}(P_k) \hat{\delta}(p_i - P_k) dP_k. \quad (\text{A1})$$

As indicated by expression (32), and recalled hereafter, the IB force is then linearized in the vicinity of  $P_m$ :

$$\mathbf{G}(P_k) = \mathbf{G}(P_m) + (P_k - P_m) \frac{\partial \mathbf{G}}{\partial P}(P_m). \quad (\text{A2})$$

Combining (A1) and (A2) leads to

$$A = \mathbf{G}(P_m) \int_{\mathbf{X}_k \in \Gamma} \hat{\delta}(p_i - P_k) dP_k + \frac{\partial \mathbf{G}}{\partial P}(P_m) \int_{\mathbf{X}_k \in \Gamma} (P_k - P_m) \hat{\delta}(p_i - P_k) dP_k. \quad (\text{A3})$$

Using the variable  $r = P_k - p_i$ , and recalling the identities  $\int r \hat{\delta}(r) dr = 0$  and  $\int \hat{\delta}(r) dr = 1$ ,  $A$  becomes

$$A = \mathbf{G}(P_m) + \frac{\partial \mathbf{G}}{\partial P}(P_m) (p_i - P_m). \quad (\text{A4})$$

Substituting  $A$  in expression (31),  $\mathcal{I}[\mathcal{S}(\mathbf{G})]$  can be expressed as

Two other kernel functions, called  $\hat{\delta}'$  and  $\hat{\delta}''$ , have been widely used in prior works. They are defined as

$$\hat{\delta}'(r) = \begin{cases} \frac{1}{3}[1 + \sqrt{1 - 3r^2}], & |r| \leq \frac{1}{2} \\ \frac{1}{6}(5 - 3|r| - \sqrt{-2 + 6|r| - 3r^2}), & \frac{1}{2} < |r| < \frac{3}{2} \\ 0, & |r| \geq \frac{3}{2} \end{cases} \quad (\text{B1})$$

$$\hat{\delta}''(r) = \begin{cases} \frac{1}{8}(3 - 2|r| + \sqrt{1 + 4|r| - 4|r|^2}), & |r| \leq 1 \\ \frac{1}{8}(5 - 2|r| - \sqrt{-7 + 12|r| - 4|r|^2}), & 1 < |r| < 2 \\ 0, & |r| \geq 2 \end{cases} \quad (\text{B2})$$

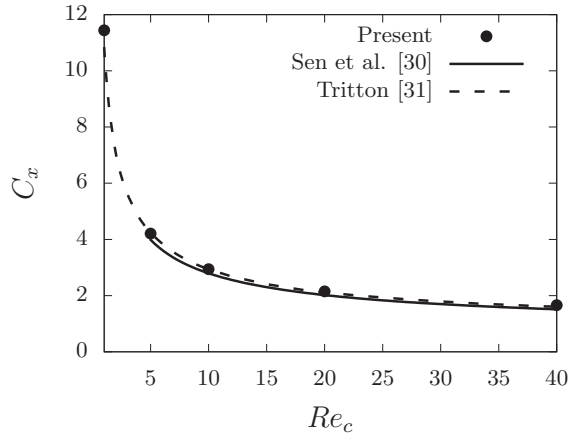


FIG. 10. Evolution of the drag force exerted on a cylinder immersed in a cross flow, as a function of the Reynolds number. The results issued from the present corrected IB method are compared to those reported in prior works of Sen *et al.* [30] and Tritton [31]. The cylinder diameter is  $D_c = 10\Delta n$ .

The first function  $\hat{\delta}'$  has been proposed by Roma *et al.* [29]. It is very similar to the kernel function employed in this work (16), with  $d = 3/2$ ; the value of  $\kappa$  is the same, namely,  $\kappa = 1/2$ . In some cases, a broader kernel function is recommended. This can be achieved using the second function  $\hat{\delta}''$ , proposed by Peskin [17]. Using this function, the value  $\kappa = 3/8$  should be used for the IB-forcing correction.

### APPENDIX C: DRAG FORCE ON A CYLINDER IMMERSED IN A CROSS FLOW

The flow past a fixed cylinder immersed in a cross flow has been extensively studied during the last decades. This

configuration is similar to the towed-cylinder system analyzed in Sec. IV C, as both systems are related by a Galilean transformation. However, the towed-cylinder system is subjected to boundary effects related to the streamwise periodicity of the computational domain. These effects are particularly important for low Reynolds numbers, as the flow is highly elliptic in these cases. Even though these effects are physically consistent, they limit the possible comparison with prior works on fixed cylinders.

In order to provide additional validation results on the flow over a cylinder, simulations have been performed in the fixed-cylinder case. The cylinder of diameter  $D_c = 10\Delta n$  is immersed in a square computational domain of dimensions  $L_x = L_y = 100D_c$ . The position of the body is fixed to  $(x_c, y_c) = (L_x/4, L_y/2)$ . A velocity Dirichlet condition is set on the left boundary of the domain, and a pressure Dirichlet condition is set on the right boundary. Periodic boundary conditions are set on the upper and lower boundaries.

Figure 10 shows the evolution of the drag force coefficient  $C_x$  as a function of the Reynolds number based on the cylinder diameter and oncoming flow velocity. The value of  $Re_c$  is varied by changing the value of the relaxation time, which ranges from 0.5375 to 2. Based on their accurate body-fitted simulations of the flow past a cylinder at low Reynolds numbers, Sen *et al.* [30] proposed an empirical function for the evolution of the viscous and pressure parts of  $C_x$ , called  $C_{xv}$  and  $C_{xp}$  ( $C_x = C_{xv} + C_{xp}$ ), in the range  $Re \in [6, 40]$ :

$$C_{xv} = -0.016 + 4.938Re^{-0.60}, \quad (C1a)$$

$$C_{xp} = 0.583 + 4.311Re^{-0.64}. \quad (C1b)$$

The drag coefficient computed with Eq. (C1), as well as that issued from the experimental work of Tritton [31], are shown in Fig. 10. A good agreement is found with the drag coefficient predicted by the corrected IB method, supporting the reliability of the present method.

- [1] Z. Guo and C. Shu, *Lattice Boltzmann Method and Its Applications in Engineering* (World Scientific, Singapore, 2013), Vol. 3.
- [2] T. Krüger, H. Kusumaatmaja, A. Kuzmin, O. Shardt, G. Silva, and E. M. Viggien, *The Lattice Boltzmann Method: Principles and Practice* (Springer, New-York, USA, 2017).
- [3] S. Chen and G. D. Doolen, *Annu. Rev. Fluid. Mech.* **30**, 329 (1998).
- [4] Y. H. Qian, D. d'Humières, and P. Lallemand, *Europhys. Lett.* **17**, 479 (1992).
- [5] X. Shan, X.-F. Yuan, and H. Chen, *J. Fluid. Mech.* **550**, 413 (2006).
- [6] S. Chapman and T. G. Cowling, *The Mathematical Theory of Non-Uniform Gases* (Cambridge University Press, Cambridge, UK, 1952).
- [7] X. He, Q. Zou, L.-S. Luo, and M. Dembo, *J. Stat. Phys.* **87**, 115 (1997).
- [8] P. L. Bhatnagar, E. P. Gross, and M. Krook, *Phys. Rev.* **94**, 511 (1954).
- [9] D. J. Holdych, D. R. Noble, J. G. Georgiadis, and R. O. Buckius, *J. Comput. Phys.* **193**, 595 (2004).
- [10] P. Lallemand and L.-S. Luo, *Phys. Rev. E* **61**, 6546 (2000).
- [11] I. Ginzburg, F. Verhaeghe, and D. d'Humières, *Commun. Comput. Phys.* **3**, 519 (2008).
- [12] D. d'Humières and I. Ginzburg, *Comput. Math. Appl.* **58**, 823 (2009).
- [13] D. P. Ziegler, *J. Stat. Phys.* **71**, 1171 (1993).
- [14] I. Ginzbourg and P. M. Adler, *J. Phys. II (France)* **4**, 191 (1994).
- [15] I. Ginzburg and D. d'Humières, *Phys. Rev. E.* **68**, 066614 (2003).
- [16] J. Latt, B. Chopard, O. Malaspinas, M. Deville, and A. Michler, *Phys. Rev. E* **77**, 056703 (2008).
- [17] C. S. Peskin, *Acta Numer.* **11**, 479 (2002).
- [18] R. Mittal and G. Iaccarino, *Annu. Rev. Fluid. Mech.* **37**, 239 (2005).
- [19] Z.-G. Feng and E. E. Michaelides, *J. Comput. Phys.* **195**, 602 (2004).
- [20] X. D. Niu, C. Shu, Y. T. Chew, and Y. Peng, *Phys. Lett. A* **354**, 173 (2006).
- [21] J. Wu and C. Shu, *J. Comput. Phys.* **228**, 1963 (2009).
- [22] T. Seta, R. Rojas, K. Hayashi, and A. Tomiyama, *Phys. Rev. E* **89**, 023307 (2014).

- [23] J. Favier, A. Revell, and A. Pinelli, *J. Comput. Phys.* **261**, 145 (2014).
- [24] G. Le and J. Zhang, *Phys. Rev. E* **79**, 026701 (2009).
- [25] Z. Chai, B. Shi, Z. Guo, and F. Rong, *J. Non-Newton. Fluid* **166**, 332 (2011).
- [26] D. N. Siebert, L. A. Hegele, and P. C. Philippi, *Phys. Rev. E* **77**, 026707 (2008).
- [27] Z. Guo, C. Zheng, and B. Shi, *Phys. Rev. E* **65**, 046308 (2002).
- [28] Z. Li, J. Favier, U. D'Ortona, and S. Poncet, *J. Comput. Phys.* **304**, 424 (2016).
- [29] A. M. Roma, C. S. Peskin, and M. J. Berger, *J. Comput. Phys.* **153**, 509 (1999).
- [30] S. Sen, S. Mittal, and G. Biswas, *J. Fluid Mech.* **620**, 89 (2009).
- [31] D. J. Tritton, *J. Fluid Mech.* **6**, 547 (1959).